# A Surgical Robotic System for Long-Bone Fracture Alignment: Prototyping and Cadaver Study

Marzieh S. Saeedi-Hosseiny, Fayez Alruwaili, Sean McMillan, Iulian Iordachita, *Senior Member, IEEE*, and Mohammad H. Abedin-Nasab

***Abstract*—In this paper, we design, develop, and validate a surgical robotic system, entitled Robossis, to assist long-bone fracture reduction, i.e., alignment, surgeries. Unlike traditional long-bone fracture surgeries, Robossis enables the surgeon to precisely align the fractured bone in the presence of large traction forces and torques. The proposed surgical system includes a novel 3-armed robot, a bone-gripping mechanism, and a master controller. The 6-DOF 3-armed wide-open parallel robot has a unique architecture, which facilitates positioning the bone inside the robot, providing a large workspace for surgical maneuvers. Kinematic analysis shows that the symmetric 3-armed mechanism provides a significant advantage over the Gough-Stewart platform, i.e., 15 times larger rotational workspace, which is a vital advantage for fracture alignment. Theoretical and experimental testing are performed to demonstrate Robossis performance, including high accuracy and force insertion capabilities. A successful cadaver test was performed using a Robossis prototype, which shows that guided by intraoperative X-ray imaging, Robossis is able to manipulate bone in all translational and rotational directions while encountering the muscle payload surrounding the femur. Robossis is designed to balance accuracy, payload, and workspace, and its innovative design presents major advantages over the existing robot designs for the reduction of long-bone fractures.**

***Index Terms*—Cadaver testing, fracture reduction, long-bone fractures, parallel mechanisms, robot design, robotic surgery.**

## I. Introduction

LONG-BONE fractures account for more than half of all fractures [1], [2]. Globally, an estimated 1.0–2.9 million femoral shaft fractures occur every year due to motor vehicle accidents [3], [4], and in the U.S., there are 430,000 proximal femur and femoral shaft fractures annually [5], [6]. Due to the aging population, this number is increasing with a CAGR of 5% and is anticipated to double by the year 2050. Current methods for treating long-bone fractures are primarily composed of three steps: positioning the patient on a surgical bed or a fracture table, manually reducing the fracture by the surgical team, and fixing the bone using plates and intramedullary (IM) nails [7]–[9].

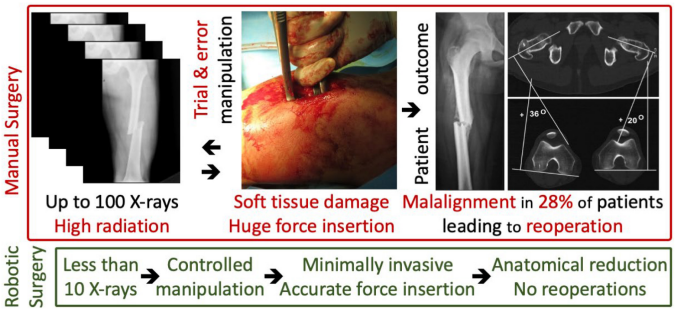


Fig. 1. Advantages of the proposed robotic surgery to align long-bone fractures compared to current manual surgery. The limitations of the current method include huge force insertion, the use of up to 100 intraoperative X-ray images, and a trial-and-error approach, which causes malalignment in 28% of patients and leads to reoperation [11], [49]–[51].

Current long-bone fracture surgeries are performed manually, and a major limitation with current protocols lies in the realignment, which presents difficulties due to the bone's elongated anatomy and the need to overcome the strength of the surrounding counteracting muscles [8]–[11]. The fracture ends are usually far from the distal and proximal joint attachments and are free to move with very limited restrictions [12]–[19]. This necessitates that surgeons and medical staff exert a high traction force to pull the bone fragments together. The surgical team must rely on experience and limited visual feedback from consecutive 2D C-Arm fluoroscopic images while trying to align the fragments in 3D. This trial-and-error approach raises the risk of physical overshoot, unnecessary soft tissue damage during the manipulation process [20]–[22], and malalignment-related complications (Fig. 1).

Furthermore, the devices currently used for traction during surgery may cause nerve palsies, numbness, and soft tissue injury. Rotational malalignment is a serious complication with long-bone fractures, with a malalignment of 15° or more after femur fracture fixation occurring in 28% of patients [23]. This is the second most common reason that orthopedic surgeons

Manuscript received August 26, 2021; revised October 22, 2021; accepted November 13, 2021. Date of publication November 19, 2021; date of current version February 22, 2022. This article was recommended for publication by Associate Editor S. Wang and Editor P. Dario upon evaluation of the reviewers' comments. This work was supported in part by the National Science Foundation (NSF) under Grant 2005570, and in part by the New Jersey Health Foundation (NJHF) under Grant PC 62-21. *(Corresponding author: Mohammad H. Abedin-Nasab.)*

Marzieh S. Saeedi-Hosseiny is with the Electrical and Computer Engineering Department, Rowan University, Glassboro, NJ 08028 USA (e-mail: saeedi64@rowan.edu).

Fayez Alruwaili and Mohammad H. Abedin-Nasab are with the Biomedical Engineering Department, Rowan University, Glassboro, NJ 08028 USA (e-mail: alruwa16@rowan.edu; abedin@rowan.edu).

Sean McMillan is with the School of Osteopathic Medicine, Rowan University, Stratford, NJ 08084 USA, and also with Virtua Willingboro Hospital, Virtua Health System, Willingboro, NJ 08046 USA (e-mail: smcmillan@virtua.org).

Iulian Iordachita is with the Laboratory for Computational Sensing and Robotics, Johns Hopkins University, Baltimore, MD 21218 USA (e-mail: iordachita@jhu.edu).

Digital Object Identifier 10.1109/TMRB.2021.3129277

are sued. Malalignment can lead to leg-length discrepancies, abnormal gait, and potential tertiary effects. Patients may require additional surgery, far more invasive than had the first surgery been performed correctly, which increases blood loss, length of hospital stay, hospital costs, and risk of complications.

Due to the limitations of manual surgery to reduce long-bone fracture, robotic surgery is a potential option with benefits to improve patient outcomes. To date, researchers have studied three different mechanisms for robots to reduce long-bone fractures, including a (1) serial mechanism, (2) parallel mechanism, and (3) serial-parallel hybrid mechanism (Table I).

Prior to 2012, researchers were interested in developing robots with a serial mechanism that would assist in reducing long-bone fractures [10], [20], [21], [24]–[26]. In 2004, a group from Regensburg Clinical University presented a serial robot system, RepoRobo, with a two-finger gripper mechanism [20]. The presented system was shown to be able to insert a maximum force of 240 N and successfully reduce bone in a benchtop model. A similar industrial robot system was further developed in 2006 and 2009, which incorporated imaging software, a navigation surgical system, and a control unit. The robot was tested on mice and human bones [10], [21], [25]. However, many limitations prevented the serial robot from being completely successful in reducing long-bone fractures. For example, due to the robot's serial connection structure, the system was unable to produce the force needed to withstand large muscle loads and reduce bone fractures [27], [28]. Also, the robot's extensive motion space created challenges in the operating room layout [27], [28].

More recently, parallel robots have become more widely tested than serial robots due to their higher precision, stability, and load-carrying capability [29]–[42]. Several researchers studied the well-known 6-armed Gough-Stewart parallel robot for the closed reduction of long-bone fractures. Since the Gough-Stewart mechanism has a restricted rotation as well as limited dexterous workspace [27], [28], [40], it has not been successfully used to reduce long-bone fractures [41], [42]. Li *et al.* developed a robot based on the Gough-Stewart platform coupled to a hydraulic cylinder and showed that it was able to insert a very large force of more than 1000 N [29], [30], [32], [35]. The same group proposed a master-slave teleoperation robot to enable surgeons to adjust the reduction's velocity and path during the surgical procedure [29], [30], [32], [35]. However, limitations of their proposed system include a large size and a limited rotational workspace of $\pm 13^\circ$ in the x- and y-directions and $\pm 17^\circ$ in the z-direction [27].

Researchers have combined the advantages of both serial and parallel structures by building a robot with a parallel-serial hybrid structure. Ye *et al.* proposed a 6-DOF serial-parallel hybrid reduction robot that presents a large workspace: a rotational workspace of $\pm 30^\circ$ in the x- and z-direction and $\pm 15^\circ$ in the y-direction and a translation workspace of $\pm 75$ mm in the x- and z-direction and $\pm 100$ mm in the y-direction [43]–[45]. However, the presented robot only grabs the bone from the distal end, which could affect the outcome of the surgical procedure [43]–[45]. More recently, Dagnino *et al.* presented a novel robot structure to reduce bone fractures while preventing soft tissue and nerve damage [46]–[48]. The researchers attached the Gough-Stewart platform to a serial robotic arm and performed a cadaver experiment. Despite the high accuracy achieved, the robot could not provide the forces needed to reduce the broken bone. As the applied force increased, the system deformed [46].

TABLE I
ROBOT-ASSISTED LONG-BONE FRACTURE REDUCTION.GOUGH-STEWART PLATFORM (GSP), SERIAL (S), PARALLEL (P),HYBRID (H), AND NOT REPORTED (NR)

| Year | Researchers | Type of Mechanism | Subject Study | Max Load (N) |
|---|---|---|---|---|
| 2004 | B.Füchtmeier et al [20] | S, Stäubli RX130 | Bone Model | 240 |
| 2004 | K Seide. et al [39] | P, GSP | Human Model | NR |
| 2006 | Westphal R. et al [26] | S, Stäubli RX90 | Human cadaver | <300 |
| 2008 | Oszwald M. et al [21] | S, Stäubli RX90 | Rat Model | 250 |
| 2009 | Westphal R. et al [10] | S, Stäubli RX90 | Bone Model | <300 |
| 2010 | Markus Oszwald. et al [25] | S, Stäubli RX90 | Human Cadaver | <300 |
| 2013 | Peifu Tang, et al [31] | P, GSP | Animal Bone | NR |
| 2012 | Ruihua Ye, et al [45] | S-P-H | Bone Model | 600 |
| 2013 | Junqiang Wang. et al [33] | P, GSP | Human Cadaver | NR |
| 2014 | Tianmiao Wang, et al [36] | P, GSP | Bone Model | 2460 |
| 2017 | Changsheng Li, et al [35] | P, GSP | Animal Bone | 1243 |
| 2016 | Giulio Dagnino, et al [61] | S-P-H | Human Cadaver | <300 |
| 2021 | T. Essomba, et al [34] | P, GSP | Bone Model | NR |

Despite many attempts (Table I), no robot has yet been successful in assisting long-bone fracture surgery. This is mainly due to the lack of an adequate robotic design that can properly address the needs for this application, including huge force insertion capabilities, high precision, and a large surgical workspace. In our previous works, we introduced and theoretically simulated 3- and 4-armed parallel mechanisms to address the challenges faced in long-bone fracture surgeries. The theoretical analysis, covering the rotational and dexterous workspace, singularity, and dynamic performance, illustrated the advantage of the mechanisms compared to the Gough-Stewart platform [49]–[53]. In the present study, we further improve the design by optimizing the structure of Robossis. In the new robot design the arms are positioned in a symmetric configuration to enlarge the rotational workspace and increase the stability. To validate our robot's capability for the specific application of long-bone fracture reduction, we discuss the results of the performed laboratory and cadaver tests. This paper is organized as follows; Section II describes the wide-open 3-armed parallel mechanism; Section III provides the theoretical analysis; and Section IV explains the experimental tests including the workspace, fracture alignment, and

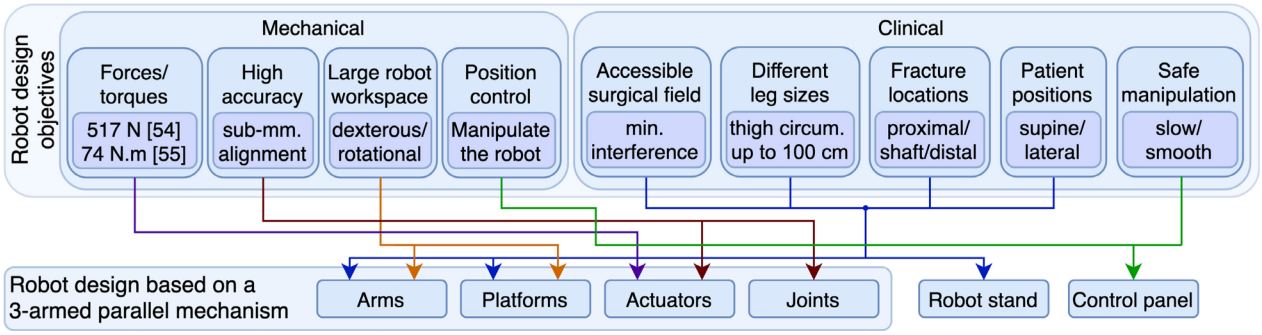


Fig. 2. Clinical and mechanical criteria to design a robot to assist long-bone fracture reduction surgeries, based on a 6-DOF 3-armed parallel mechanism. The robot design needs to be able to insert the required forces and be able to manipulate the fractured bone with high accuracy in a large workspace. Also, the design of the robot should be compatible with the different sizes of the patient's leg, the location / type of fracture, and provide an accessible surgical field for the surgeon to perform the surgical procedure.

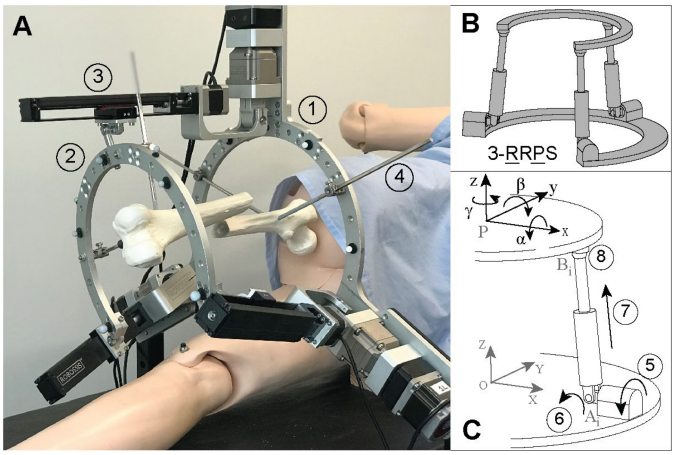


Fig. 3. Illustration of the 6-DOF 3-armed Robossis, a surgical robot for long-bone fracture reduction. (A) The mechanism consists of (1) a fixed platform, (2) a moving platform, and (3) three arms. (4) Bone gripping system, which attaches the robot's rings to the fractured bone through half-pin rods. (B) The robot utilizes a 6-DOF 3-RRPS parallel mechanism. (C) Each leg consists of (5) an active and (6) a passive rotary joint, (7) an active prismatic joint, and (8) a passive spherical one. The center of the moving ring has 3 translational (x, y, z) and 3 rotational ($\alpha$, $\beta$, $\gamma$) motions.

cadaveric study. In Section V, we discuss the results, followed by a conclusion in Section VI.

## II. Robot Architecture

### A. Mechanical and Clinical Criteria

Robots used for fracture reduction must be precise, able to apply large amounts of force, and provide 6 degrees of freedom (DOF) control [8]. In addition, these robots must provide surgeons with an accessible surgical field, ample workspace, and the ability to perform safe manipulation (Fig. 2). To achieve such a robot, we designed a unique mechanism that provides the robot with the clinical and mechanical specifications required for bone fracture reduction surgery (Fig. 3). The forces and torques required to reduce a fracture are determined based on a local coordinate system located in the center of the femoral fracture [54], [55].

The maximum force along the medial-lateral axis (x-axis) was 203 N and the maximum forces along the anterior-posterior axis (y-axis) and the femoral shaft (z-axis) were 517 N and 505 N, respectively. The maximum torques around the y-axis and the x-axis were calculated to be 16.4 N·m and 38.3 N·m, respectively, and the maximum torque around the front axis was 74 N·m [54], [55]. Therefore, the designed robot must withstand forces up to 517 N and torques up to 74 N·m to be suitable for long-bone fracture reduction surgeries. The final desired position for the fractured bone segments is anatomical alignment. To avoid malalignment and malrotation, the assisting robot should be able to achieve alignment with submillimeter accuracy.

Additionally, a key mechanical requirement for a robot assisting in long-bone fracture reduction is a large workspace and high maneuverability to provide an accessible and safe manipulation for the surgeon. As such, the design of Robossis rings and arrangement of its actuators are placed so that a maximum desirable dexterous/rotational workspace is achieved. The final desired position for the fractured bone is anatomical alignment. To avoid malalignment and malrotation, the assisting robot should be able to achieve alignment with submillimeter accuracy. To achieve the stated, Robossis gearboxes have low backlash of less than 5 arcmin and robot components have been manufactured with high accurate machine tools to avoid clearances between the moving joints.

### B. 3-Armed 6-DOF Parallel Robot

Given the required mechanical and clinical criteria, a unique design of Robossis to reduce long-bone fractures is proposed (Fig. 3A). The architecture of Robossis, with its low number of arms in a symmetric configuration, enables it to easily grip and manipulate cylindrical objects such as long bones. The robot's open-ring structure precisely grabs the leg while providing free range of motion for varying surgical maneuvers. As shown in Fig. 3B, Robossis has a parallel mechanism in which a fixed platform and a moving platform are connected by three robot arms. Cartesian coordinates A(O, X, Y, Z) and B(P, x, y, z) represented by {A} and {B} are attached to the base and moving platforms, respectively. The robot utilizes a 6-DOF 3-RRPS parallel mechanism, where each leg consists of an active and a passive rotary joint, an active prismatic joint, and a passive spherical joint. The center of the moving ring has

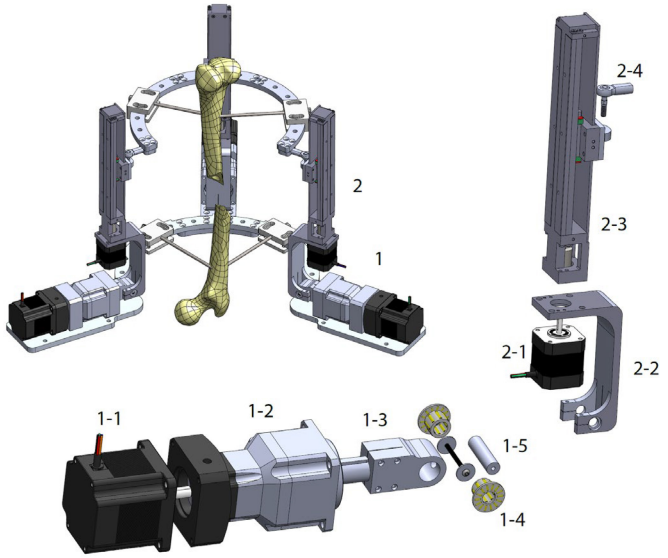


Fig. 4. Robossis lower (1) and upper (2) arms are equipped with a (1-1) Autonics-A8K stepper motor, (1-2) apex 60:1 gearbox, (1-3) universal joint, (1-4) roller bearing and thrust roller bearing, (1-5) rod, bolt, nuts and washer, (2-1) Autonics-A3K stepper motor, (2-2) lower arm, (2-3) Hiwin KK40 linear guide, and (2-4) spherical joint.

3 translational (x, y, z) and 3 rotational ($\alpha$, $\beta$, $\gamma$) motions (Fig. 3C).

Each arm consists of three joints; universal, prismatic, and spherical (Fig. 4). A rotary and linear actuator are used to actuate each arm. The lower rotary actuators, Autonics-A8K stepper motors, are attached to the semicircle on the fixed platform. The shafts of the lower rotary actuators are attached to the linear actuators through universal joints. The spherical joints connect the upper parts of the linear actuators to the moving rings. The Autonics-A8K stepper motor has a maximum torque of 0.83 N·m operated at 1.4 A/phase.

The Autonics-A8K is attached to a gearbox, Apex Dynamics, with a reduction ratio of 60:1 and low backlash of less than 5 arcmin. The gearbox increases the max holding torque to 48.6 N·m for each arm, which results in total torque of 145.8 N·m for the whole mechanism. The gearbox shaft is connected to the lower part of the arm using a revolute joint, which is made of a needle bearing. Linear actuation at each arm is provided using a Hiwin KK40 linear guide with a 1.0 mm pitch. The linear actuator is powered by an 80W Autonics-A3K stepper motor with a maximum torque of 0.24 N·m, which results in a maximum insertable linear force of 1527 N at each arm. Therefore, using the A3K microstepper, the proposed Robossis can exert up to 4559 N of force in the z-direction.

Robossis features a mechanism for gripping the fractured bone fragments and can insert sufficient force, as theoretically estimated, to reduce long-bone fractures. Standard half-pin rods are the connecting device between the robot rings and the bone fragments. These rods are currently being used in other orthopedic applications, such as external fixator devices, and are designed to withstand the existing large payloads.

## III. Theory and Analysis

### A. Inverse Kinematics

In this section, inverse kinematic equations of the proposed symmetric and non-symmetric 3-armed mechanisms are derived. Given the desired position and orientation of the end-effector, the length of the linear actuator $d_i$ and the rotation of the active joint $\theta_i$ are to be computed [53], [56]–[58]. *A(O,x,y,z)* and *B(P,u,v,w)* are the Cartesian coordinate frames attached to the fixed and moving platforms and they are represented by $\{A\}$ and $\{B\}$, respectively (Fig. 3C). Referring to Fig. 3C, $\boldsymbol{a}_i$ and ${}^B\boldsymbol{b}_i$ represents $OA_i$ and $PB_i$, respectively. $\boldsymbol{a_i} = g\begin{bmatrix} cos\gamma_i & sin\gamma_i & 0 \end{bmatrix}^T$ and ${}^B\boldsymbol{b}_i = h\begin{bmatrix} cos\gamma_i & sin\gamma_i & 0 \end{bmatrix}^T$, where $g$ and $h$ are the radii of the fixed and moving platforms, respectively. $\gamma_i$ is the arm attachment angle as shown in Fig. 5. The rotation matrix from $\{B\}$ to $\{A\}$, ${}^A_BR = [r_{ij}]$, using Euler angles are represented as

$$ {}^A_BR = \begin{bmatrix} c\beta c\gamma & -c\beta s\gamma & s\beta \\ c\gamma s\beta s\alpha + s\gamma c\alpha & -s\gamma s\beta s\alpha + c\gamma c\alpha & -c\beta s\alpha \\ -c\gamma s\beta c\alpha + s\gamma s\alpha & s\gamma s\beta c\alpha + c\gamma s\alpha & c\beta c\alpha \end{bmatrix}, \tag{1} $$

where $c\alpha = cos\alpha$ and $s\alpha = sin\alpha$, and so on. $\alpha$, $\beta$, and $\gamma$ are the three Euler angles defined according to the *x*-*y*-*z* convention. Thus, the vector ${}^B\boldsymbol{b}_i$ would be expressed in the fixed frame $\{A\}$ as $\boldsymbol{b}_i = {}^A_BR\ {}^B\boldsymbol{b}_i$.

Vector $\boldsymbol{d}_i$, which represents $A_iB_i$, can be written as

$$ \boldsymbol{d_i} = \boldsymbol{p} + \boldsymbol{b_i} - \boldsymbol{a_i}, \tag{2} $$

where $\boldsymbol{p} = \begin{bmatrix} x & y & z \end{bmatrix}^T$, which denotes the position vector of the center of the moving platform. Therefore, $\boldsymbol{d}_i$ can be rewritten as

$$ \boldsymbol{d_i} = \begin{bmatrix} x - x_i \\ y - y_i \\ z - z_i \end{bmatrix}, \tag{3} $$

in which

$$ \begin{cases} x_i = -h(c\gamma_i\ r_{11} + \ s\gamma_i\ r_{12}) + g\ c\gamma_i \\ y_i = \ -h(c\gamma_i\ r_{21} + \ s\gamma_i\ r_{22}) + g\ s\gamma_i \\ z_i = \ -h(c\gamma_i\ r_{31} + s\gamma_i\ r_{32}) \end{cases}. \tag{4} $$

Using (3), the length of the linear actuator $d_i$ can be calculated as

$$ d_i = \sqrt{(x - x_i)^2 + (y - y_i)^2 + (z - z_i)^2}. \tag{5} $$

Coordinates $C_i(A_i,x_i,y_i,z_i)$ are attached to the fixed platform with their $x_i$ axes aligned with the rotary actuators and $z_i$ axes perpendicular to the fixed platform.

Thus, vector $\boldsymbol{d_i}$ can be expressed in $\{C_i\}$ as

$$ {}^{C_i}\boldsymbol{d_i} = d_i \begin{bmatrix} s\psi_i \\ -s\theta_i c\psi_i \\ c\theta_i c\psi_i \end{bmatrix}. \tag{6} $$

Using (6), vector $\boldsymbol{d_i}$ can be expressed in $\{A\}$ as

$$ \boldsymbol{d_i} = {}^A_{C_i}R\ {}^{C_i}\boldsymbol{d_i}, \tag{7} $$

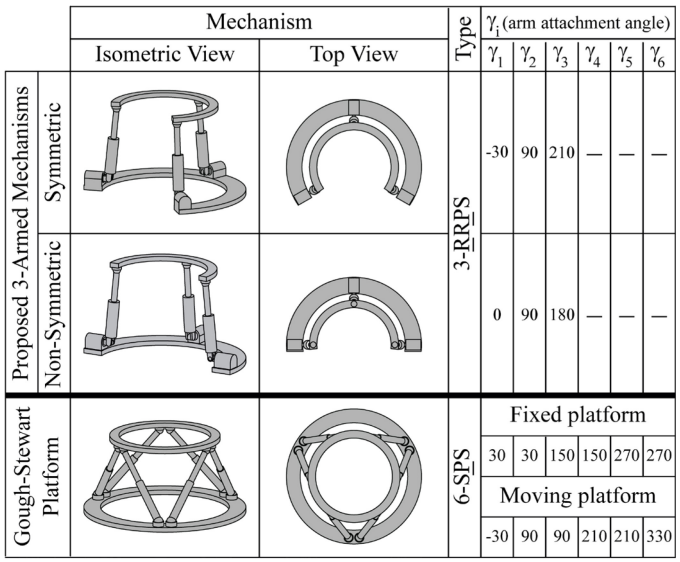


Fig. 5. Arm structure and attachment angles ($\gamma$i) of the proposed 3-armed mechanisms and Gough–Stewart platform. We compared the dexterous workspace for the three mechanisms. From top to bottom, the dexterous workspaces of the mechanisms are 66270, 66190, and 27072 cm$^3$, respectively.

where ${}^{A}_{C_i}R$ is the rotation matrix from $\{C_i\}$ to $\{A\}$,

$$ {}^{A}_{C_i}R = \begin{bmatrix} c\gamma_i & -s\gamma_i & 0 \\ s\gamma_i & c\gamma_i & 0 \\ 0 & 0 & 1 \end{bmatrix}. \tag{8} $$

By equating (7) and (3), the rotation of the active joint $\theta_i$ is obtained as

$$ \theta_i = \sin^{-1}\left(\frac{sin\gamma_i(x - x_i) - cos\gamma_i(y - y_i)}{d_i cos\psi_i}\right). \tag{9} $$

As a result, the value of the active joints of the 3-armed mechanisms can be calculated using (4) and (9). The only difference in the inverse kinematic solution for the proposed symmetric and non-symmetric mechanisms is in the arm attachment angle $\gamma_i$, which is shown in Fig. 5.

### B. Workspace Comparison

To investigate the kinematic performance of the two different configurations of Robossis mechanisms, we study their rotational workspace in comparison with the well-known Gough-Stewart mechanism. For this analysis, the three mechanisms are assumed to be constructed with an architecture shown in Fig. 5. During simulation, the endpoint effector of each mechanism is assumed as a point (P), and is fixed at the center of the workspace, where all linear actuators are at their center range. Then, we simulate the orientation of point P by steps of 5° to obtain a theoretical representation of the rotational workspace for all three mechanisms.

Euler angles $\alpha 1$, $\alpha 2$, and $\alpha 3$ are used based on the X−Y−Z convention. At each step, the extension of the mechanism actuators is measured and verified to be within a possible range for the actuators, in order to include the corresponding set of $\{\alpha 1, \alpha 2, \alpha 3\}$ in the rotational workspace. As illustrated in Fig. 6, the proposed symmetric 3-armed parallel mechanism has a 15 times larger rotational workspace compared to that of the Gough–Stewart mechanism. To handle different types of femur fracture, the robot needs such high rotational capabilities to provide a vital advantage in fracture alignment. We can see also non-symmetric mechanism has more than 7 times larger rotational workspace compared to Gough-Stewart platform.

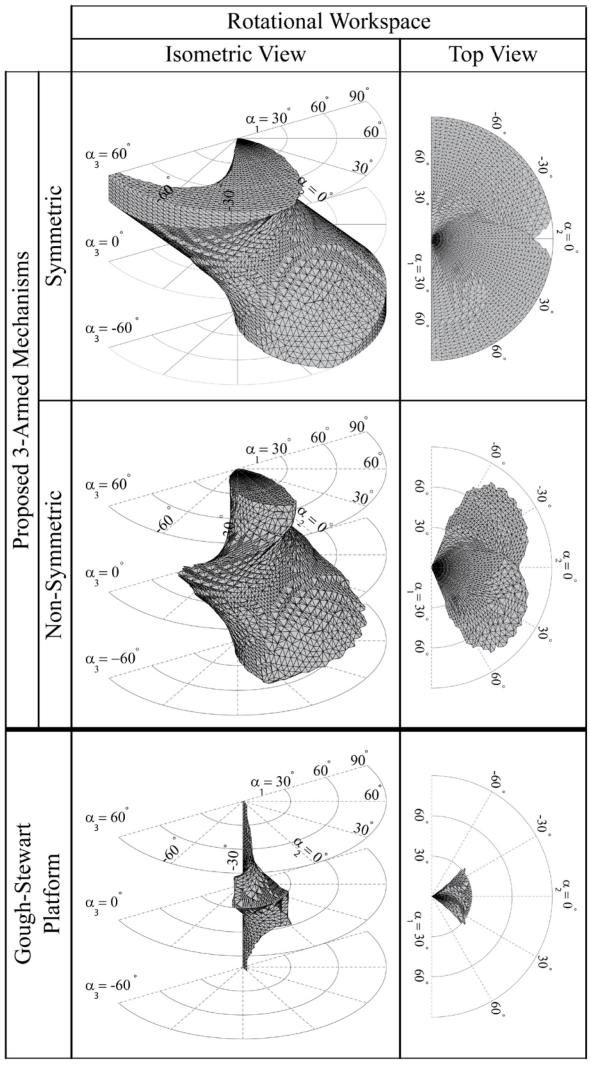


Fig. 6. Rotational workspaces of the symmetric and non-symmetric design of a 6-DOF 3-armed parallel mechanism compared to the well-known Gough-Stewart mechanism. At zero yaw ($\alpha 3$) angle, the symmetric 3-armed design can reach pitch ($\alpha 2$) rotations of up to +/−90° combined with roll ($\alpha 1$) rotations of up to 90°, while these values are, respectively, +/−30° and 30° for the Gough-Stewart platform. Based on different types of long-bone fracture, the robot needs high rotational capabilities that are significantly met in the proposed symmetric parallel mechanism. The rotational workspaces of the three mechanisms, from top to bottom, are 2.71, 1.32, and 0.18 (rad$^3$), respectively. The proposed symmetric 3-armed mechanisms has a significantly larger workspace compared to the two others.

## IV. Surgical Robot Subsystems

### A. Control Panel

We develop a control panel interface to manipulate the robot moving platform with smooth and low-speed motions in 6 DOF (3 translations and 3 rotations). The surgeon can use

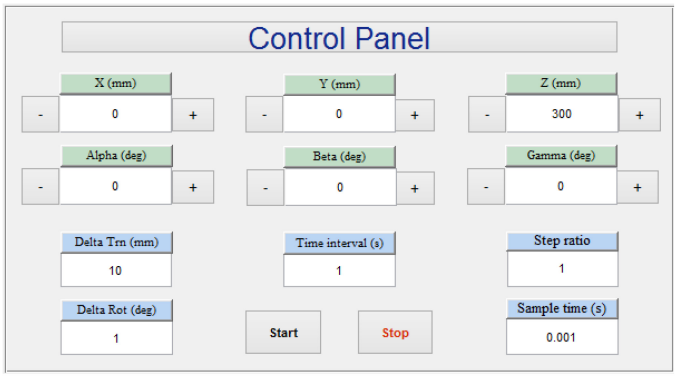


Fig. 7. Concept for the control panel graphical user interface (GUI). The user is able to manipulate the robot in all 6 DOF while imposing the desired time interval.

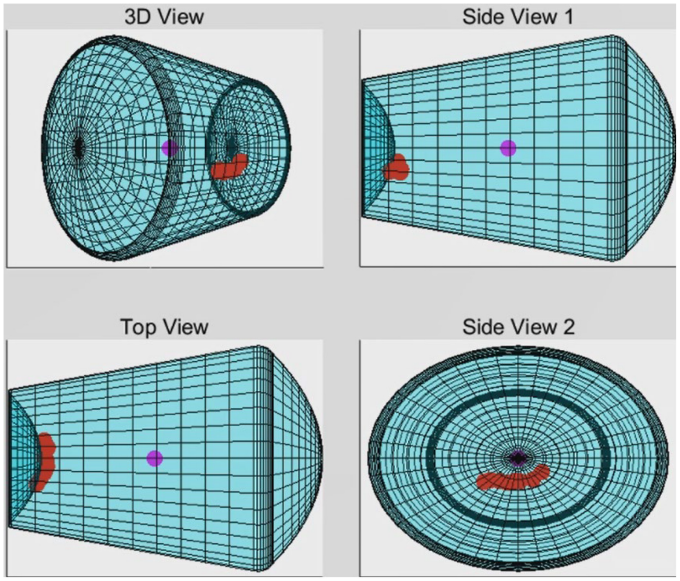


Fig. 8. Multiple views of the workspace. The purple and red dots denote the initial and real-time positions of the robot's end-effector, respectively. The blue cylinder shows the boundaries of the robot's dexterous workspace. The bottom left image clearly illustrates how the Falcon force-feedback controller restricts the movements of the end-effector inside the workspace.

the control panel to direct the robot's moving platform, bring the robot to the home position, and enact an emergency stop.

The control panel also includes step ratio, degree interval and time interval that can be adjusted to increase precision according to the user's needs. This panel provides the user with a precise and smooth way to manipulate the fracture (Fig. 7).

A new graphical user interface (GUI) is developed to allow the positions and rotations to be controlled, show real-time data from optical trackers, and compare the error between the data derived from the kinematics model of the robot (desired position) to that of the optical trackers (actual position). Each axis has an original, change, and final position/rotation. The change and final values can be manipulated by typing in new numbers. The GUI allows multiple changes to be entered but not implemented until a "Start" button is touched.

### *B. Master Controller*

We control the movements of the presented robot prototype using the Falcon 3D Haptic Controller (Fig. 8). The workspace has a cone shape with five sections. The Falcon provides haptic feedback based on a boundary setup within MATLAB, while sending its current position to MATLAB for processing. When these coordinates are on the boundary, the device provides force feedback and moves the user's hand back inside the boundary region. This way, the surgeon will stay inside the workspace.

To deliver the required force feedback and DOF, we develop different codes to connect the Falcon to the robotic system; (1) a gravity code, which enables the Falcon to maintain position while force is not applied, (2) a cylinder code that forms artificial borders to the workspace, and (3) a viscosity code that applies a small opposing force. This viscosity force prevents sudden movements from affecting the overall position, which results in higher accuracy.

To show the importance of the viscosity function, we performed tests on the gravity and viscosity code. A weight of 106 g was tied to the end of the Falcon's handle and was then pulled to the max height of the workspace. This results in a force of 1.04 N to emulate a user's hand operating the device. The time it took the Falcon's handle to fall to the bottom of the workspace was then recorded using the gravity code first and then the viscosity code. On average for the gravity code, it took 0.31 s for the weight to fall to the bottom of the workspace, and on average for the viscosity code, it took 4.2 s. This shows the oversensitivity of the gravity code, which can cause issues during surgery if the user were to accidentally hit the handle or apply too much force. For this reason, the viscosity code is a useful and necessary addition to the master controller code. This test was then replicated multiple times with different weights to collect more data on the viscosity and gravity performance difference.

To address speed, we develop a computer algorithm that is compatible with slow movements for long-bone reduction surgery. We use a speed threshold of 2 mm/s and eliminate faster movements.

### *C. Bone Gripping System*

We design a passive mechanism to easily attach/detach the bone-gripping system to the moving and fixed platform using knob grip screws. This allows the surgeon to attach the gripping mechanism to the robot, intra-operatively, after attaching it to the fragments. The design requirements include the ability to grip main bone fragments and withstand traction forces of more than 500 N without damaging or breaking the bone fragment after force insertion. The robot requires a precise mechanism for adhering to the fractured bone fragments that will be attached to the rings.

An important consideration is to keep the femoral canal open so that the surgeon can pass the IM nail through it in the fixation step while the robot holds the bone fragments in place. Providing a stable attachment is also critical to prevent damage to the bone, soft tissue, muscles, and nerves. The unicortical

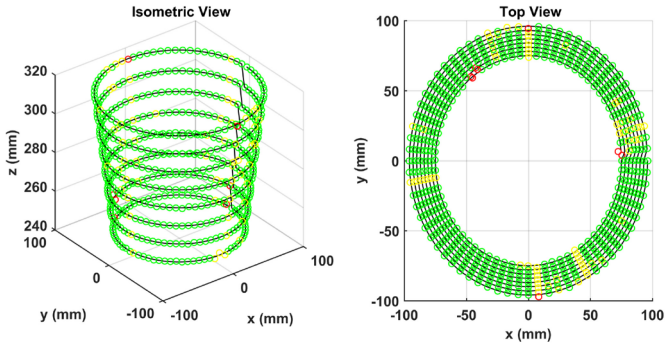


Fig. 9. Experimental testing of the workspace presented as deviation points, the difference between the desired and measured location read by the Optitrack systems. Colors: green = deviation < 0.5 mm, yelow = 0.5 mm < deviation < 1.5 mm, and red = deviation > 1.5 mm.

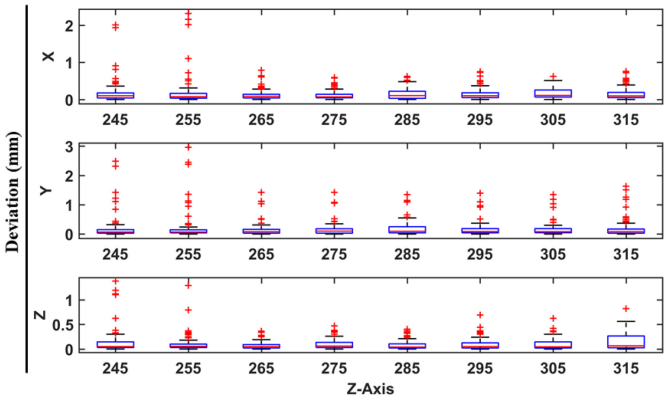


Fig. 10. Box plots illustrate the deviation of the robot in the workspace testing. Maximum deviations of 2.3 mm (X-direction), 3.0 mm (Y-direction), and 1.4 mm (Z-direction) were observed.

half-pin option (with flat, not blunted, tips) as a direct attachment is a promising option. Half-pins are either self-drilling or pre-drilling.

Seitz, Jr. *et al.* studied the pin purchase between the two groups and found that self-drilled pins at a depth of 10 mm and pre-drilled pins at a depth of 4 mm had a comparable purchase that is sufficient for external fixation [59]. Croker *et al.* report that the average cortical thickness of the femoral midshaft is approximately 50% [60]. If a cortical thickness of 50% is assumed on ∼30 mm diameter cadaver bones, this equates to ∼7.5 mm of purchase depth for the half-pins, which is almost double the required purchase depth for pre-drilled pins, while falling short of the purchase depth for self-drilling pins.

So, we use self-tapping half-pin rods as the gripping system for the presented surgical robot. These rods are attached to the fixed and moving platforms via angled pin connectors (Fig. 3A).

## V. Pre-Clinical Testing and Results

### A. Workspace Testing

We performed workspace testing to determine the accuracy of the Robossis end effector in reaching different locations in the dexterous workspace. During the experiment, the desired dexterous workspace locations were generated in a circular pattern every 5° and increased in height and radius by 10 mm and 3 mm. The generated data points were fed into the inverse kinematics model, and the location of the endpoint effector was tracked using stereoscopic vision system (Optitrack Flex 13, tolerance = 0.5 mm, Frame Rate: 30-120 FPS NaturalPoint, Inc. DPA OptiTrack). Markers were placed in a specific location and orientation on the fixed and moving rings of the robot, using two Optitrack cameras placed above the robot to capture the movements. Results of the workspace testing shown in Fig. 9 illustrate the high accuracy of the robot in reaching the desired locations of the workspace, with an average error of 0.324 mm. Furthermore, boxplots shown in Fig. 10 illustrate the deviation in the workspace testing in the X-, Y-, and Z-directions. The presented symmetric mechanism is able to reach all of the generated points with maximum deviations of 2.3 mm (X-direction), 3.0 mm (Y-direction), and 1.4 mm (Z-direction) (Fig. 10).

### B. Benchtop Femur Fracture Alignment

To test the performance of the proposed robot, we performed an experiment using a broken plastic model of the femur to align the broken parts of the bone by Robossis. Four half-pin surgical rods were drilled into the midshaft of the broken femur, two in the proximal part and two in the distal segment. The surgical rods were then connected to the fixed and moving platforms using angled pin connectors. We cut the bone with a saw to create a transverse fracture. Next, the distal femur fragment was displaced from the proximal fragment to resemble a practical fracture. Then, we aligned the femur fragments by controlling the robot movements in 6 DOF using our touch screen control panel. Figure 11 presents the steps taken to align the femur fracture. In the first step (A to B), moving ring rotated the bone $-5°$ in the $\alpha$-direction. Next step (B to C) was $+5°$ rotation in the â-direction. Afterward (C to D), we rotated the bone $-10°$ in the $\gamma$-direction. Then (D to E), $-20$ mm displacement in the Y-direction happened and from E to F, we had $-20$ mm displacement in the X-direction. Finally (F to G), the robot shifted the distal bone $-20$ mm in the Z-direction. This experiment demonstrates that Robossis can successfully manipulate the bone fragments in 6 DOF in space, in a smooth and controlled way.

### C. Cadaveric Testing

Guided by X-ray images taken by a C-Arm, a femur shaft fracture reduction surgery was conducted on an 85-year-old male cadaver using the Robossis mechanism (Fig. 12). Results of testing showed that Robossis is able to manipulate bone in all translational (X-Y-Z) and rotational ($\alpha$-$\beta$-$\gamma$) directions while encountering the muscle payload surrounding the femur. During the reduction, the distal bone fragment was manipulated in all directions to test the functionality of Robossis and then realigned with the proximal fragment (Fig. 13). Robossis was able to insert the needed traction forces to extend the fractured bone segments as well as significantly rotate the distal bone fragments. Thus, the large rotational workspace was validated as well as the ability to manipulate long bones in a precise and controlled manner in the space. It should be noted that no noticeable deflection of the robotic arms was observed.

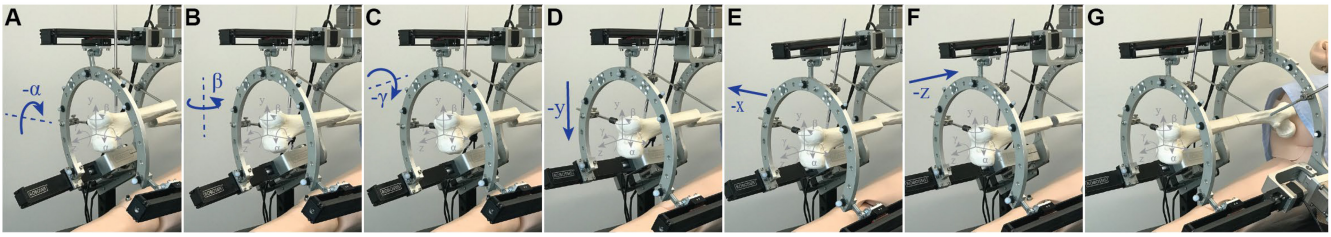


Fig. 11. Demonstration of bone reduction in 6 DOFs: (A to B) Rotation of $-5°$ in the $\alpha$-direction. (B to C) Rotation of $+5°$ in the $\beta$-direction. (C to D) Rotation of $-10°$ in the $\gamma$-direction. (D to E) Displacement of $-20$ mm in the y-direction. (E to F) Displacement of $-20$ mm in the x-direction. (F to G) Displacement of $-20$ mm in the z-direction.

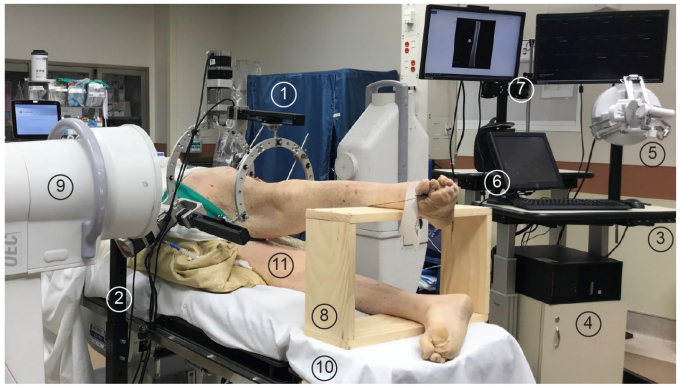


Fig. 12. Robossis setup and cadaver testing. (1) Robossis attached to (2) its height-adjustable stand. The surgeon workstation consists of (3) a compact dual-tier cart, (4) control hardware, (5) 7-DOF force-feedback master controller (Sigma.7), (6) touchscreen control panel, and (7) two monitors. (8) A leg holder stabilizes the foot. (9) A C-Arm takes X-ray images intraoperatively. The robot fits inside (10) a normal surgical bed. (11) Cadaver, an 85-year-old man, in the lateral position.

The surgeon was able to access the fracture site, maneuver around the operating room, and use C-Arm regularly without interference.

Robossis is compatible with the C-Arm since a standard C-Arm has an opening of 0.8 m, which allows for rotation around the patient's limb while robot is attached to the limb. During the test, the C-Arm was able to obtain images at angles of 0° (full lateral) and 60° without the intervention of the robot arms (Fig. 13). We took 54 intraoperative X-ray images of the fractured bone using a c-arm, although improved planning should be able to reduce this number and increase the available angles for viewing.

A preliminary bone gripping test was also performed on a cadaver. Using self-drilling self-tapping external fixation pins, the surgeon could successfully attach the cadaver's femur fragments to the Robossis platforms. The surgeon drilled two half-pin rods in the cadaver's femur, one in the proximal segment and one in the distal bone fragment. The rods were efficient in bearing the loads of the bone manipulation by the robot throughout the test. Although the cadaver was an 85-year-old male, we could successfully attach the half-pin rods without any extra fracture. In addition, the bone could withstand the forces exerted by the robot during the test run. The bone-gripping mechanism of Robossis provides localized manipulation of the distal bone fragment while maintaining other proximal bone fragments stable. The gripping system was shown to be effective in controlling the rotation, elongation/distraction, and alignment capabilities of the fracture through robotic assistance (confirmed under direct visualization and fluoroscopy).

The robot stand is compatible with a typical surgical bed, as it has a width of 0.5 m and an adjustable height from 0.57 m to 1 m. The Robossis stand can slide onto the standard surgical bed with a clearance of 0.05 m on both sides.

## VI. Discussion

To complete the reduction of a long-bone fracture, the proximal and distal bone fragments must be manipulated and returned to their correct anatomical position while the surgeon is exerting large forces (∼500 N) to overcome the surrounding muscular traction forces. For this application, we have been able to successfully present the design, development, theoretical analysis, and experimental testing of a 6-DOF 3-armed parallel robot. The feasibility of the system was theoretically and experimentally evaluated through the workspace simulation, experimental testing of the workspace, benchtop femur fracture alignment, and cadaveric testing.

Mechanism design is a key issue in any robotic application. Our new 6-DOF 3-armed robot satisfies clinical and mechanical design requirements. To manipulate the bone fragments, the robot needs to be highly maneuverable. In contrast, a limited workspace restricts the possibility of placing the patient at the surgeon's discretion, which leads to greater risks of injury to the patient and reduced efficiency of the surgeon's performance. The theoretical simulation showed that the Robossis symmetric and non-symmetric mechanisms have a significant advantage over the Gough-Stewart platform, with 15x and 7x larger rotational workspace, respectively. Further, testing demonstrates that Robossis can reach the most extreme points in the workspace while maintaining minimal deviation from those points.

The benchtop femur fracture alignment test was a practical demonstration and synthesis of the proposed robot's straight-line accuracy and configuration accuracy. By simply distracting and then realigning the femur fractures, the robot qualitatively shows efficient and precise reduction. Furthermore, the results of the cadaver experiment illustrate the capability of Robossis to reduce femur fractures under immense muscle forces. Guided by X-ray images taken by C-Arm intraoperatively, Robossis was able to successfully manipulate the bones in all translational (X-Y-Z) and rotational

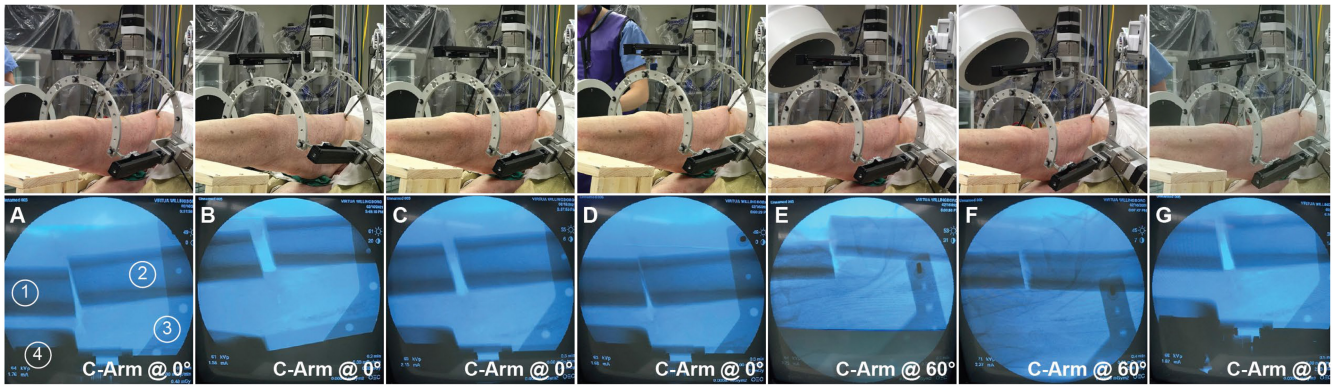


Fig. 13. Demonstration of the robot capabilities for fracture reduction in a cadaveric experiment at Virtua hospital. The robot was attached to the fractured (1) proximal and (2) distal femur fragments. As our gripping mechanism, one biocritical pin was drilled into each fragment to attach the bone to the rings of the robot. We used (3) a marker to identify the bone movements in the X-ray images. We were able to take X-rays using the C-Arm at 0° and 60°, while the robot was attached to the cadaver, without interference of the robot arms. (4) A part of the robot arm is seen in lower left corner of the images when the C-Arm is in full lateral 0°. A total of 59 steps were executed by the robot to test different maneuvers. Some are as follows: (A to B) $+15°$ in the $\gamma$-direction and $-30$ mm in the z. This step demonstrates the force insertion capability to extend and rotate the fragments in the presence of muscle traction forces. (B to C) $-15°$ in the $\gamma$-direction and $-10$ mm in the z-direction. (C to D) $-10$ mm in the y-direction and $-10$ mm in the z-direction. The X-ray image of the C-Arm at 0° shows the fragment ends are aligned and adjacent. (E) The robot remained at the previous position, while the C-Arm rotated to 60° to check the alignment. (E to F) $-15$ mm in the y-direction. The X-ray image shows reduction from 60° angle. (G) The robot remained at the previous position while the C-Arm rotated to 0° to check the alignment. The X-rays from both angles validate reduction in 3D space.

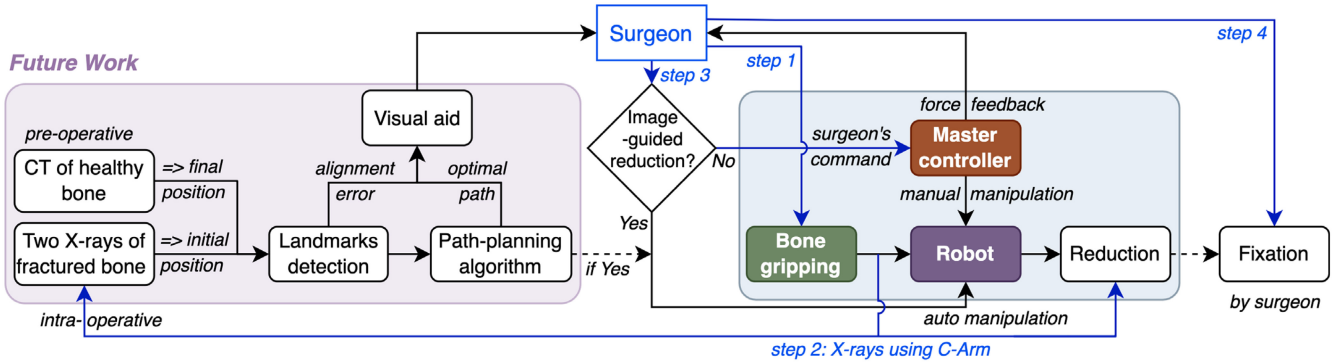


Fig. 14. Illustration of the proposed Robossis-assisted surgical flow. Current work focuses on development of the robot, its bone-gripping system, and a force-feedback master controller for the surgeon. In future work, a path-planning algorithm, which utilizes key femur landmarks, will be developed to aid the surgeon in image-guided reduction of the fractured bone.

($\alpha$-$\beta$-$\gamma$) directions to place the bone to its correct anatomical alignment.

C-Arm could take images at angles of 0° (full lateral) and 60°, while the robot was attached to the limb, to determine the relative position of the bone fragments. These images were captured without any interference of Robossis arms. During surgery, X-ray images are very critical in monitoring the fracture and success in the reduction.

A limitation of this early test is an undesired movement of the Robossis moving platform due to the weight of the patient's leg, although only during movements along the upward vertical direction. This indicates the need for a stronger gearbox and perhaps a harness to support and stabilize the distal portion of the leg.

The presented robot-assisted surgical flow integrates four critical subsystems including the master controller, the 3-armed robot, the bone-gripping mechanism, and the imaging software (Fig. 14).

This research lays the groundwork for future work to automate long-bone reduction with an innovative image-guided surgical system. Imaging software will be utilized to develop a path-planning algorithm to assist the surgeon in finding the optimal path to anatomically reduce the long-bone fracture with sub-millimeter accuracy. Two X-ray images will be used to identify the broken bone's main landmarks and subsequently determine the relative position of the main parts of the bone in space. In addition, unbroken bone CT information will be used to find the final anatomical location of the fractured bone. As a result, the robot will autonomously follow the optimal path to align the long-bone fragments with sub-millimeter accuracy under the surgeon's supervision. The robot will hold the fragments in the correct final position until the surgeon fixes the fracture.

In our further work, the commercial Sigma.7 (Force Dimension) haptic controller will be integrated to Robossis based on its parallel structure and high fidelity. Sigma.7 provides 6-DOF force feedback plus 1 DOF for gripping, along with high force insertion, high precision, and large workspace. The master controller will be a critical component of the surgeon's console to control the robot during the surgical procedure while providing the muscle force feedback. Surgeons will utilize the master controller to manipulate Robossis in

all 6 DOF and subsequently realign the bone fragments. To further investigate the force insertion capabilities of the robot, extensive laboratory and cadaver experiments with different fracture types and locations will be performed. Additionally, the bone gripping mechanism will be optimized and quantitatively tested using 3 or 4 (bicortical and/or unicortical) half-pins on cadavers to study their alignment accuracy. Cuffs or braces could be considered with elderly patients, pediatric patients, or those with osteoporosis.

## VII. Conclusion

The analytical and experimental tests conducted in this study confirm the ability of Robossis surgical system to assist long-bone fracture reduction surgeries, using its unique mechanism features. Robossis has significant advantages over the alternative parallel mechanisms presented in the literature, including fewer number of arms, which significantly increases the workspace, reduces the weight and inertial effects, and provides a wider accessible surgical field for the surgeon. The designed control panel enables the surgeon to manipulate the bone fragments in a smooth and precise manner, while the Robossis gripping system grabs the bone segments tightly with no extra damage to the bone. Therefore, Robossis as a superior orthopedic surgical system can assist surgeons in long-bone fracture reduction surgeries.

## References


[1] C. M. Court-Brown and B. Caesar, "Epidemiology of adult fractures: A review," *Injury*, vol. 37, no. 8, pp. 691–697, Aug. 2006, doi: 10.1016/j.injury.2006.04.130.

[2] L. Rennie, C. M. Court-Brown, J. Y. Q. Mok, and T. F. Beattie, "The epidemiology of fractures in children," *Injury*, vol. 38, no. 8, pp. 913–922, Aug. 2007, doi: 10.1016/j.injury.2007.01.036.

[3] K. J. Agarwal-Harding, J. G. Meara, S. L. M. Greenberg, L. E. Hagander, D. Zurakowski, and G. S. M. Dyer, "Estimating the global incidence of femoral fracture from road traffic collisions: A literature review," *J. Bone Joint Surg.*, vol. 97, no. 6, p. e31, 2015.

[4] O. Johnell and J. A. Kanis, "An estimate of the worldwide prevalence and disability associated with osteoporotic fractures," *Osteoporos. Int.*, vol. 17, no. 12, pp. 1726–1733, 2006.

[5] A. C. Ng *et al.*, "Trends in subtrochanteric, diaphyseal, and distal femur fractures, 1984–2007," *Osteoporos. Int.*, vol. 23, no. 6, pp. 1721–1726, 2012.

[6] N. Enninghorst, D. McDougall, J. A. Evans, K. Sisak, and Z. J. Balogh, "Population-based epidemiology of femur shaft fractures," *J. Trauma Acute Care Surg.*, vol. 74, no. 6, pp. 1516–1520, 2013.

[7] P. R. Wolinsky, E. McCarty, Y. Shyr, and K. Johnson, "Reamed intramedullary nailing of the femur: 551 cases," *J. Trauma Acute Care Surg.*, vol. 46, no. 3, pp. 392–399, 1999.

[8] T. Gosling *et al.*, "Robot-assisted fracture reduction: A preliminary study in the femur shaft," *Med. Biol. Eng. Comput.*, vol. 43, no. 1, pp. 115–120, 2005.

[9] J. Buschbaum, R. Fremd, T. Pohlemann, and A. Kristen, "Computer-assisted fracture reduction: A new approach for repositioning femoral fractures and planning reduction paths," *Int. J. Comput. Assist. Radiol. Surg.*, vol. 10, no. 2, pp. 149–159, 2015.

[10] R. Westphal *et al.*, "Robot-assisted long bone fracture reduction," *Int. J. Robot. Res.*, vol. 28, no. 10, pp. 1259–1278, 2009.

[11] R. L. Jaarsma and A. Van Kampen, "Rotational malalignment after fractures of the femur," *J. Bone Joint Surg. [Br],* vol. 86, no. 8, pp. 1100–1104, 2004.

[12] M. D. Neuman *et al.*, "Nerve block use after hip fracture versus elective hip or knee arthroplasty: Retrospective analysis," *J. Amer. Geriatrics Soc.*, vol. 68, no. 4, pp. 835–840, 2020.

[13] K. P. Connolly, R. S. Kleinman, K. L. Stevenson, M. D. Neuman, and S. N. Mehta, "Delirium reduced with intravenous acetaminophen in geriatric hip fracture patients," *J. Amer. Acad. Orthop. Surg.*, vol. 28, no. 8, pp. 325–331, 2020.

[14] M. W. Hast, M. Chin, E. C. Schmidt, J. Sanville, G. K. Van Osten, and S. Mehta, "Mechanical effects of bone substitute and far-cortical locking techniques in 2-part proximal humerus fracture reconstruction: A cadaveric study," *J. Orthop. Trauma*, vol. 34, no. 4, pp. 199–205, 2020.

[15] K. Pirruccio, S. Mehta, and N. P. Sheth, "The association between newly accredited orthopedic residency programs and teaching hospital complication rates in lower extremity total joint arthroplasty," *J. Surg. Educ.*, vol. 77, no. 3, pp. 690–697, 2019.

[16] B. Schultz *et al.*, "Orthopedic surgeons have inadequate knowledge of the cost of trauma-related imaging studies," *Orthopedics*, vol. 42, no. 5, pp. e454–e459, 2019.

[17] T. O. McKinley, F. A. Lisboa, A. D. Horan, G. E. Gaski, and S. Mehta, "Precision medicine applications to manage multiply injured patients with orthopaedic trauma," *J. Orthop. Trauma*, vol. 33, pp. S25–S29, Jun. 2019.

[18] M. Stark, D. DeBernardis, C. McDowell, E. Ford, and S. McMillan, "Percutaneous skeletal fixation of painful subchondral bone marrow edema utilizing an injectable, synthetic, biocompatible hyaluronic acid–based bone graft substitute," *Arthrosc. Techn.*, vol. 9, no. 11, pp. e1645–e1650, Nov. 2020, doi: 10.1016/j.eats.2020.07.005.

[19] E. Ford, M. DeFrance, and S. McMillan, "Arthroscopic medial meniscus transplant utilizing a multi-technique fixation," *Strat. Campus Res. Day*, vol. 23, pp. 48–49, May 2019.

[20] B. Füchtmeier *et al.*, "Reduction of femoral shaft fractures in vitro by a new developed reduction robot system'RepoRobo"' *Injury*, vol. 35, pp. A113–A119, Jun. 2004.

[21] M. Oszwald *et al.*, "A rat model for evaluating physiological responses to femoral shaft fracture reduction using a surgical robot," *J. Orthop. Res.*, vol. 26, no. 12, pp. 1656–1659, 2008.

[22] N. Hawi *et al.*, "Navigated femoral shaft fracture treatment: Current status," *Technol. Heal. Care*, vol. 20, no. 1, pp. 65–71, 2012.

[23] R. L. Jaarsma, D. F. M. Pakvis, N. Verdonschot, J. Biert, and A. Van Kampen, "Rotational malalignment after intramedullary nailing of femoral fractures," *J. Orthop. Trauma*, vol. 18, no. 7, pp. 403–409, 2004.

[24] S. Kuang *et al.*, "A novel passive/active hybrid robot for orthopaedic trauma surgery," *Int. J. Med. Robot. Comput. Assit. Surg.*, vol. 8, no. 4, pp. 458–467, 2012, doi: 10.1002/rcs.1449.

[25] M. Oszwald *et al.*, "Robot-assisted fracture reduction using three-dimensional intraoperative fracture visualization: An experimental study on human cadaver femora," *J. Orthop. Res.*, vol. 28, no. 9, pp. 1240–1244, 2010.

[26] R. Westphal *et al.*, "A surgical telemanipulator for femur shaft fracture reduction †," *Int. J. Med. Robot. Comput. Assist. Surg.*, vol. 2, pp. 238–250, Sep. 2006, doi: 10.1002/rcs.81.

[27] L. Bai, J. Yang, X. Chen, Y. Sun, and X. Li, "Medical robotics in bone fracture reduction surgery: A review," *Sensors*, vol. 19, no. 16, 2019, p. 3593, doi: 10.3390/s19163593.

[28] J. X. Zhao, C. Li, H. Ren, M. Hao, L. C. Zhang, and P. F. Tang, "Evolution and current applications of robot-assisted fracture reduction: A comprehensive review," *Ann. Biomed. Eng.*, vol. 48, no. 1, pp. 203–224, 2020, doi: 10.1007/s10439-019-02332-y.

[29] H. Du *et al.*, "Advancing computer-assisted orthopaedic surgery using a hexapod device for closed diaphyseal fracture reduction," *Int. J. Med. Robot. Comput. Assist. Surg.*, vol. 11, no. 3, pp. 348–359, 2015.

[30] P. Tang, T. Wang, and L. Hu, "Long-bone fracture-reduction robot," U.S. Patent 9 610 101, 2017.

[31] P. Tang, L. Hu, H. Du, M. Gong, and L. Zhang, "Novel 3D hexapod computer-assisted orthopaedic surgery system for closed diaphyseal fracture reduction," *Int. J. Med. Robot. Comput. Assist. Surg.*, vol. 8, no. 1, pp. 17–24, 2012.

[32] C. Li *et al.*, "A novel master-slave teleoperation robot system for diaphyseal fracture reduction: A preliminary study," *Comput. Assist. Surg.*, vol. 21, pp. 163–168, 2016, doi: 10.1080/24699322.2016.1240304.

[33] J. Wang, W. Han, and H. Lin, "Femoral fracture reduction with a parallel manipulator robot on a traction table," *Int. J. Med. Robot. Comput. Assist. Surg.*, vol. 9, no. 4, pp. 464–471, 2013.

[34] T. Essomba and S. N. Phu, "Kinematic analysis and design of a six-degrees of freedom 3-RRPS mechanism for bone reduction surgery," *J. Med. Device*, vol. 15, no. 1, p. 15, 2021, doi: 10.1115/1.4049057.

[35] C. Li *et al.*, "Accuracy analysis of a robot system for closed diaphyseal fracture reduction," *Int. J. Adv. Robot. Syst.*, vol. 11, no. 10, p. 169, 2014.

[36] T. Wang *et al.*, "A removable hybrid robot system for long bone fracture reduction," *Biomed. Mater. Eng.*, vol. 24, no. 1, pp. 501–509, 2014.

[37] L. Hu *et al.*, "A femur fracture reduction method based on anatomy of the contralateral side," *Comput. Biol. Med.*, vol. 43, no. 7, pp. 840–846, 2013.
[38] K. Majidifakhr, S. Kazemirad, and F. Farahmand, "Robotic assisted reduction of femoral shaft fractures using Stewart platform," in *Proc. MMVR*, 2009, pp. 177–179.
[39] K. Seide, M. Faschingbauer, M. E. Wenzl, N. Weinrich, and C. Juergens, "A hexapod robot external fixator for computer assisted fracture reduction and deformity correction," *Int. J. Med. Robot. Comput. Assist. Surg.*, vol. 01, no. 1, p. 64, 2004, doi: 10.1581/mrcas.2004.010101.
[40] M. H. Abedinnasab, F. Farahmand, and J. Gallardo-Alvarado, "A 3-legged parallel robot for long bone fracture alignment," in *Proc. ASME Int. Design Eng. Tech. Conf. Comput. Inf. Eng. Conf.*, 2017, p. 11.
[41] C. Gosselin and J. Angeles, "Singularity analysis of closed-loop kinematic chains," *IEEE Trans. Robot. Autom.*, vol. 6, no. 3, pp. 281–290, Jun. 1990, doi: 10.1109/70.56660.
[42] C. Gosselin and L. T. Schreiber, "Kinematically redundant spatial parallel mechanisms for singularity avoidance and large orientational workspace," *IEEE Trans. Robot.*, vol. 32, no. 2, pp. 286–300, Apr. 2016, doi: 10.1109/TRO.2016.2516025.
[43] S. Wang, Y. Chen, and Z. Ping, "Control simulation of a six DOF parallel-serial robot for femur fracture reduction," in *Proc. IEEE Int. Conf. Virtual Environ. Human Comput. Interfaces Meas. Syst. (VECIMS)*, 2009, pp. 330–335, doi: 10.1109/VECIMS.2009.5068919.
[44] R. Ye and Y. Chen, "Path planning for robot assisted femur shaft fracture reduction: A preliminary investigation," in *Proc. IEEE Int. Conf. Virtual Environ. Human Comput. Interfaces Meas. Syst. (VECIMS)*, 2009, pp. 113–117, doi: 10.1109/VECIMS.2009.5068876.
[45] R. Ye, Y. Chen, and W. Yau, "A simple and novel hybrid robotic system for robot-assisted femur fracture reduction," *Adv. Robot.*, vol. 26, nos. 1–2, pp. 83–104, 2012.
[46] I. Georgilas, G. Dagnino, P. Tarassoli, R. Atkins, and S. Dogramadzi, "Robot-assisted fracture surgery: Surgical requirements and system design," *Ann. Biomed. Eng.*, vol. 46, no. 10, pp. 1637–1649, 2018, doi: 10.1007/s10439-018-2005-y.
[47] G. Dagnino, I. Georgilas, P. Köhler, R. Atkins, and S. Dogramadzi, "Image-based robotic system for enhanced minimally invasive intra-articular fracture surgeries," in *Proc. IEEE Int. Conf. Robot. Autom.*, 2016, pp. 696–701, doi: 10.1109/ICRA.2016.7487196.
[48] G. Dagnino, I. Georgilas, P. Tarassoli, R. Atkins, and S. Dogramadzi, "Vision-based real-time position control of a semi-automated system for robot-assisted joint fracture surgery," *Int. J. Comput. Assist. Radiol. Surg.*, vol. 11, no. 3, pp. 437–455, 2016, doi: 10.1007/s11548-015-1296-9.
[49] M. H. Abedin-Nasab and M. S. Saeedi-Hosseiny, "Robossis: Orthopedic surgical robot," in *Handbook of Robotic and Image-Guided Surgery*. Cambridge, MA, USA: Elsevier, 2020, pp. 515–528.
[50] M. H. Abedinnasab, F. Farahmand, and J. Gallardo-Alvarado, "The wide-open three-legged parallel robot for long-bone fracture reduction," *J. Mech. Robot.*, vol. 9, no. 1, p. 10, 2017.
[51] M. H. Abedinnasab, J. G. Alvarado, B. Tarvirdizadeh, and F. Farahmand, "Sliding-mode tracking control of the 6-dof 3-legged wide-open parallel robot," in *Parallel Manipulators: Design, Applications and Dynamic Analysis*. New York, NY, USA: Nova Sci., 2016, pp. 143–166.
[52] M. S. Saeedi-Hosseiny, F. Alruwaili, A. Patel, S. Mc Millan, I. Iordachita, and M. H. Abedin-Nasab, "Spatial detection of the shafts of fractured femur for image-guided robotic surgery," in *Proc. IEEE Eng. Med. Biol. Soc.*, pp. 1–4, 2021.
[53] M. Abedin-Nasab, "Surgical robot," U.S. Patent 10 603 122, 2020.
[54] T. Gösling *et al.*, "Forces and torques during fracture reduction: Intraoperative measurements in the femur," *J. Orthop. Res.*, vol. 24, no. 3, pp. 333–338, 2006.
[55] Q. Zhu, B. Liang, X. Wang, X. Sun, and L. Wang, "Force–torque intraoperative measurements for femoral shaft fracture reduction," *Comput. Assist. Surg.*, vol. 21, pp. 37–44, Nov. 2016.
[56] M. H. Abedinnasab, F. Farahmand, B. Tarvirdizadeh, H. Zohoor, and J. Gallardo-Alvarado, "Kinematic effects of number of legs in 6-DOF UPS parallel mechanisms," *Robotica*, vol. 35, no. 12, pp. 2257–2277, 2017.
[57] M. H. Abedinnasab, Y.-J. Yoon, and H. Zohoor, "Exploiting higher kinematic performance-using a 4-legged redundant PM rather than gough-stewart platforms," *Ser. Parallel Robot Manip. Dyn. Control Optim.*, vol. 10, Mar. 2012, Art. no. 32141.
[58] M. H. Abedinnasab and G. R. Vossoughi, "Analysis of a 6-DOF redundantly actuated 4-legged parallel mechanism," *Nonlinear Dyn.*, vol. 58, no. 4, p. 611, 2009.
[59] W. H. Seitz, Jr., *et al.*, "External fixator pin insertion techniques: Biomechanical analysis and clinical relevance," *J. Hand Surg. Amer.*, vol. 16, no. 3, pp. 560–563, 1991.
[60] S. L. Croker, J. G. Clement, and D. Donlon, "A comparison of cortical bone thickness in the femoral midshaft of humans and two non-human mammals," *Homo*, vol. 60, no. 6, pp. 551–565, 2009.
[61] G. Dagnino *et al.*, "Image-guided surgical robotic system for percutaneous reduction of joint fractures," *Ann. Biomed. Eng.*, vol. 45, no. 11, pp. 2648–2662, 2017, doi: 10.1007/s10439-017-1901-x.